Earth Planet. Sci. Lett. 656 (2025) 119271

Contents lists available at ScienceDirect

Earth and Planetary Science Letters

journal homepage: www.elsevier.com/locate/epsl

Dislocation networks facilitate element diffusion in deformed garnet

B.V. Ribeiro [a,*], C.L. Kirkland [a], M.A. Finch [b], C. Yakymchuk [c], S.M. Reddy [a], F.M. Faleiros [d], K. Goemann [e], I. Belousov [f]

[a] Curtin Frontiers Institute for Geoscience Solutions, School of Earth and Planetary Sciences, Curtin University, Australia
[b] School of Geography, Earth and Atmospheric Sciences, The University of Melbourne, Australia
[c] Department of Earth and Environmental Sciences, University of Waterloo, Canada
[d] Institute of Geosciences, University of Sao Paulo, Brazil
[e] Central Science Laboratory, University of Tasmania, Australia
[f] CODES Analytical Laboratories, University of Tasmania, Australia

ARTICLE INFO

Editor by Dr A Webb

Keywords:
Garnet geochemistry
Garnet geochronology
Crystal-plastic deformation;petrochronology

ABSTRACT

Garnet is a key mineral in constraining the conditions and timing of metamorphism. Changes in its elemental composition can record distinct pressure (*P*) and temperature (*T*) conditions, and information on timing can be retained by its isotopic systems. Due to its mostly rigid behavior during deformation and high closure temperature for Lu–Hf diffusion, garnet geochemistry is interpreted to reflect garnet growth undisturbed by subsequent ductile deformation. However, nanoscale observations demonstrated element mobility into intracrystalline defects and suggested that garnet may not be as geochemically robust as commonly thought. Here, we assess the efficiency of dislocations in promoting grain-scale element mobility in garnet porphyroclasts naturally deformed under high-*T* conditions using a range of high-spatial resolution microstructural and chemical-isotopic techniques. We show that the development of low-angle subgrain boundaries in response to dislocation creep is insufficient to promote grain-scale element mobility. However, we find that Ca, Mg and trace elements (e.g., La, Ce, Lu, Hf, Sm, Ti, Zr and U) are mobilised on the grain-scale when the dislocation density exceeds the threshold to form a dislocation network. Although dislocation networks can enhance element mobility, the differences in *P*–*T* conditions from 'low'- and 'high-strain' domains are negligible and unresolvable, reinforcing its geochemical robustness to estimate the prograde garnet growth conditions. Nevertheless, dislocation networks facilitate synkinematic diffusional Hf loss and Lu gain, demonstrating that garnet intracrystalline deformation can impact the Lu–Hf geochronometer. These observations indicate that isotopic resetting in garnet is more complex than previously assumed in rocks that underwent high-strain and temperature deformation.

1. Introduction

Garnet is a common metamorphic mineral in medium- to high-temperature shear zones where it typically forms rigid porphyroclasts within a higher strain matrix (Wang and Ji, 1999). The composition of garnet (particularly in terms of major elements) is sensitive to changes in pressure and temperature (*P*–*T*) conditions, and garnet incorporates sufficient quantities of radiogenic isotopes amenable to dating (Baxter et al., 2017). These features have made garnet a key mineral in resolving the *P*–*T*–*t* history of metamorphic rocks and the orogenic belts in which they reside (Baxter and Scherer, 2013).

Intracrystalline deformation has been shown to disturb key geochronometers like zircon (Reddy et al., 2007; Piazolo et al., 2016), titanite (Papapavlou et al., 2017; Kavanagh-Lepage et al., 2022), and apatite (Ribeiro et al., 2020; Odlum et al., 2022). However, the effects of such processes on garnet are unclear due to difficulties to petrographically identify deformed garnet domains, and to carrying out in situ isotopic analysis. Garnet chemical and isotopic systems have been interpreted to reflect growth and to be undisturbed by subsequent deformation (e.g., Voegelé et al., 1998). However, nanoscale studies investigating the robustness of garnet composition to intracrystalline deformation have found that dislocations may lead to segregation of major and trace elements like Ca, Mg, Fe, Na and Ti into intracrystalline defects (Tacchetto et al., 2022; Dubosq et al., 2023, 2024), which may act as fast-diffusion pathways or trace element traps (Verberne et al., 2022). Studies focused on grain-scale chemical modifications suggest

---

* Corresponding author.
E-mail address: bruno.vieiraribeiro@curtin.edu.au (B.V. Ribeiro).

https://doi.org/10.1016/j.epsl.2025.119271
Received 12 October 2024; Received in revised form 13 January 2025; Accepted 13 February 2025

element mobility associated with intracrystalline deformation at medium- to high-*T* conditions over 500 °C (Storey and Prior, 2005; Chapman et al., 2019). However, the rarity of well-developed microstructures like subgrains and dislocation networks (Prior et al., 2000, 2002) has prevented a thorough evaluation of the extent of such recrystallisation process in garnet geochemistry.

Here, we explore the effect of intracrystalline deformation on garnet chemistry and Lu–Hf chronometry using a novel in situ technique. We combine microstructural, chemical mapping (major and trace element), texturally-controlled Lu–Hf isotopic analysis and phase equilibrium modelling to determine the role of deformation on grain-scale element mobility in garnet deformed at high-*T* conditions. Our results provide new insights into how intracrystalline deformation influences element mobility and isotopic resetting in garnet under high -strain and -temperature conditions.

2. Background

We studied garnet porphyroclasts from a high-*T* mylonitic paragneiss (sample R3–7A) within the Além Paraíba shear zone (APSZ, SE Brazil; Fig. S1, supplementary material SM[1]). The NE-trending APSZ is a dextral transcurrent shear zone within the central Ribeira Belt, an ENE-trending orogen in southeastern South America associated with the Neoproterozoic–Early Cambrian assembly of Western Gondwana (Campanha et al., 2023). The APSZ extends for ~200 km and deforms Paleoproterozoic ortho- and paragneiss from the Juiz de Fora Complex (Paraíba do Sul Terrane; Fig. S1; Giraldo et al., 2019). Conventional thermometry and titanium-in-quartz thermometry indicate regional deformation temperature ranging from 600 to 800 °C (Cavalcante et al., 2018; Giraldo et al., 2019). The timing of pre-kinematic high-*T* metamorphism spans 595–590 Ma based on zircon U–Pb dates from mylonitic ortho- and paragneiss (Giraldo et al., 2019), suggesting that the timing of shearing deformation along the APSZ took place post metamorphic peak (Heilbron et al., 2008). Monazite U–Pb dates as young as c. 550 Ma are interpreted to reflect continuous (re)crystallisation after the metamorphic peak associated with amphibolite-facies shearing and associated retrograde fluid flow (Giraldo et al., 2019).

The studied sample is a mylonitic paragneiss primarily composed of quartz (Qz), plagioclase (Pl), alkali feldspar (Afs), garnet (Gt), biotite (Bt), and ilmenite (Ilm), with compositional banding marked by Afs- and Pl-dominated ribbons (Fig. 1A and S2; mineral abbreviations after Whitney and Evans, 2010). Given the high-*T* mineral assemblages, absence of muscovite, and presence of leucocratic layering, we infer that the peak metamorphic assemblage included anatectic melt. The mylonitic matrix is defined by polygonal Qz–Pl–Afs, and the foliation is marked by Qz–Pl–Afs ribbons and a spaced Bt foliation (Fig. 1A and S2). We note the presence of interstitial Afs within Pl-dominated ribbons and as inclusions in garnet along with quartz. Subhedral garnet comprises ~5 vol. % of the rock, and are commonly wrapped by Qz–Pl–Afs ribbons to form σ-shaped porphyroclasts with asymmetric Bt tails consistent with dextral shear (Fig. 1A and S2). Garnet contains Qz, Bt, Afs, apatite and pyrrhotite inclusions, and is crosscut by fractures perpendicular to the X-direction of the finite strain ellipsoid (Fig. 1A and B). Quartz displays strong crystallographic preferred orientation with the <c>-axis close to the Y-direction of the finite strain ellipsoid, indicating recrystallisation under high-*T* and strain conditions (Fig. 1B and C; Faleiros et al., 2016).

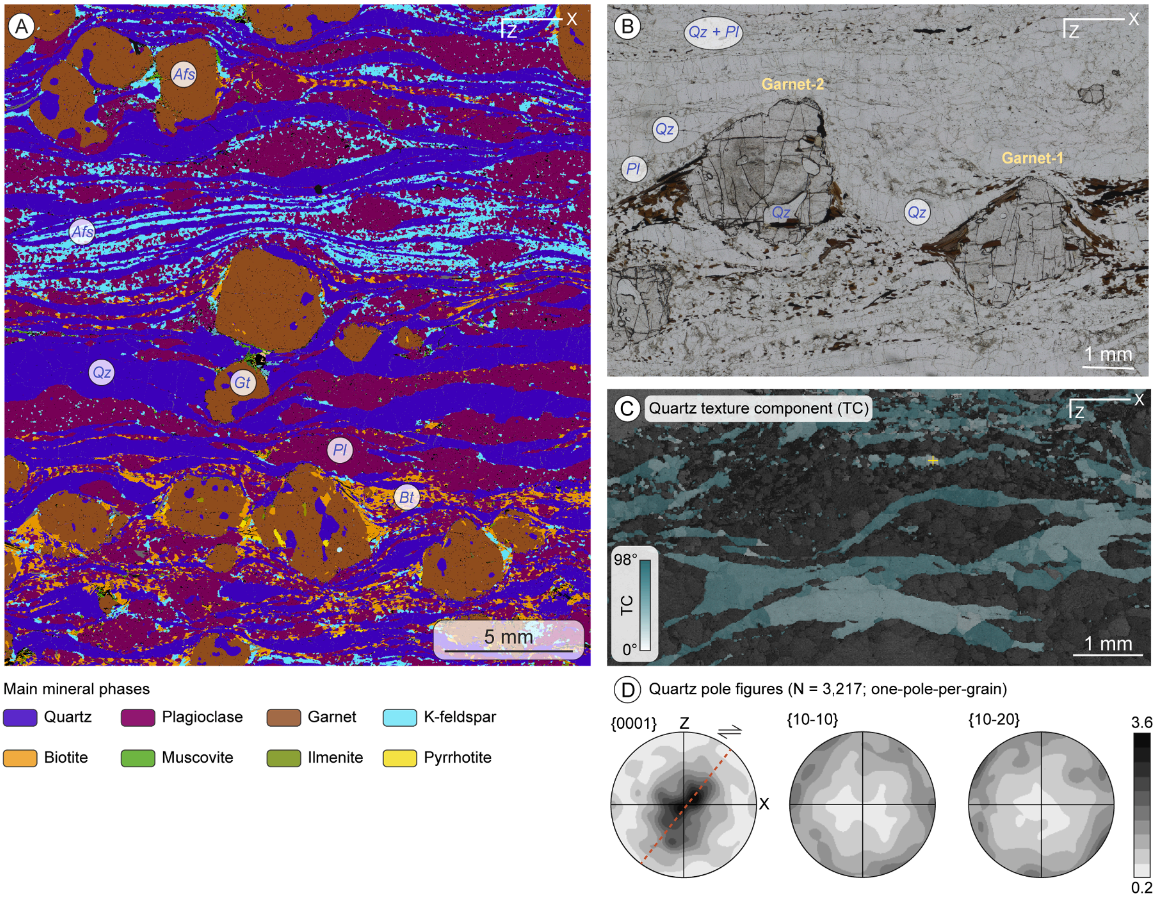

Fig. 1. A) Automated mineralogical map from the mylonitic paragneiss (sample R3–7A); B) Plane-polarized light photomicrographs of two studied garnet porphyroclasts; C) Quartz texture component map based relative to the yellow-cross; D) Quartz pole figures displayed in lower hemisphere, equal area projection with contour half-width of 15°.

3. Methods

3.1. Microstructural characterisation

Three garnet grains were selected for detailed microstructural characterisation via electron backscatter diffraction (EBSD) mapping. Crystallographic data were collected on a polished thin section cut parallel to the kinematic plain (XZ plane in the finite strain ellipse). The thin section was polished on a Buehler VibroMet II for four hours using 0.05 μm colloidal silica colloidal (ethylene glycol-based) prior to data collection. A thin carbon coat was applied to mitigate charging (~5 μm thickness). The EBSD analyses were performed using the TESCAN Clara field emission gun scanning electron microscope equipped with an Oxford Instruments Symmetry EBSD detector in the John de Laeter Centre, Curtin University. The EBSD data were collected using a 20 kV acceleration voltage, 1 nA beam current, 70° specimen tilt and variable step sizes between 1.5 and 10 μm. Data processing was carried out using the AZtecCrystal 2.1. Geometrically necessary dislocation maps (GND) were produced in the same software based on the lattice curvature measured by EBSD. The GND was calculated using a square Kernel shape with 3 × 3 pixel Kernel size, maximum angle of 10°, and an average Burger vector $\frac{1}{2}\langle 110\rangle$.

3.2. Garnet chemistry

Compositional data (major elements) were acquired at the Central Science Laboratory, University of Tasmania, on a JEOL JXA-8530F Plus field emission electron microprobe with 5 wavelength dispersive spectrometers at an accelerating voltage of 15 kV, beam current of 30 nA, and beam diameter of 2 μm. The calibration setup included analysing crystals LIFL for Mn and Fe, PETL for Ca and Ti, TAPL for Na and Mg, and TAP for Al and Si, with Kα lines being used for all elements.

Peak and background counting times were 10 ss for Na, 20 ss for Si, Ca and Ti, 30 ss for Al and Mg, and 60 ss for Mn and Fe. The background correction method was linear off-peak for Al, Ca, and Fe, and exponential for Si, Mg, Ti, Mn, and Na. Unknown and standard intensities were corrected for deadtime. The matrix correction method was PAP with the LINEMU mass absorption coefficient dataset. Elements were calibrated against natural and synthetic reference materials such as synthetic rutile for Ti, natural rhodonite for Mn, natural jadeite for Na (all P&H Developments, UK), Hematite Harvard H92649 for Fe, Plagioclase Lake County NMNH115900 for Al, wollastonite (UTas in house) for Ca, and Olivine MongOL Sh11–2 for Mg and Si. Garnet structural formulae was calculated using MinPlot (Walters, 2022) using 12-equivalent oxygens. Garnet chemistry data are available in SM[2].

X-ray elemental maps were acquired at the same spectrometer settings as above by stage scanning at a dwell time of 50 ms per pixel with a beam current of 30 nA and beam diameter of 1 μm. Only peak intensity maps were acquired and the mean atomic number method with calibration curves acquired on standards was used for background correction. The same calibration standards as above were used for quantification. Presentation output X-ray elemental maps were produced using the XMapTools platform (Lanari et al., 2014).

Trace element mapping was carried out via LA-ICP-MS analysis at CODES Analytical Laboratories facility, University of Tasmania. The analyses were conducted on RESOLution SE laser ablation system with 193 nm ArF excimer laser coupled with an Agilent 7900 quadrupole mass spectrometer. The sample ablation was performed in He atmosphere flowing at 0.35 $\mathrm{l.min^{-1}}$ and immediately combined with Ar flowing at 1.05 $\mathrm{l.min^{-1}}$. Straight nylon tubing 3 m long was used as an interface between laser ablation system and ICPMS. Whole imaged area was covered by a raster of parallel lines. Square laser beam of 9 μm was used with 9 $\mu\mathrm{m.sec^{-1}}$ rastering speed along the lines. Ablation was carried out using laser fluence of 3.5 $\mathrm{J.cm^{-2}}$ and frequency of 10 Hz. The measured analytes include ^{23}Na, ^{24}Mg, ^{27}Al, ^{29}Si, ^{31}P, ^{43}Ca, ^{45}Sc, ^{49}Ti, ^{51}V, ^{53}Cr, ^{55}Mn, ^{57}Fe, ^{66}Zn, ^{69}Ga, ^{89}Y, ^{90}Zr, ^{118}Sn, ^{139}La, ^{140}Ce, ^{146}Nd, ^{147}Sm, ^{153}Eu, ^{157}Gd, ^{163}Dy, ^{172}Yb, ^{175}Lu, ^{178}Hf, ^{208}Pb, ^{232}Th and ^{238}U. Total sweep time was equal to 0.39 s, with individual dwell time of 2 ms for major elements, and 20 ms for trace elements. The international glass NIST SRM 612 was used as a primary reference material for initial quantification and instrument drift correction, while glasses GSD-1G and BCR-2G were used as secondary reference materials. Quantification was performed using ^{27}Al as the internal standard element obtained through EPMA analysis given its homogeneous distribution across 'low'- and 'high-strain' domains (~11 wt. %), normalizing all measured cations to 100 wt. % oxide total. The LADR software was used to determine count rates (counts per second) to concentration ($\mu\mathrm{g.g^{-1}}$, ppm) conversion factors. Trace element maps were constructed using the XMapTools platform (Lanari et al., 2014) using the concentrations for each element ($\mu\mathrm{g.g^{-1}}$).

3.3. Phase equilibrium modelling

We carried out forward phase equilibrium modelling to evaluate the impact of intracrystalline deformation in the *P*–*T* conditions attained in the garnet 'low'- and 'high-strain' domains. Whole-rock major elements of sample R3–7A were analysed in fused glass disc using a Panalytical Axios Max Advanced X-ray fluorescence spectrometer (XRF) at the GeoAnalitica-USP analytical center following Mori et al. (1999). Whole-rock composition is available in SM[2], along with interlaboratory reference materials and detection limit for each measured element.

Calculations were performed using GeoPS (Xiang and Connolly, 2022) with 11 components (SiO_2–Al_2O_3–K_2O–CaO–FeO–Na_2O–MgO–MnO–TiO_2–O_2–H_2O) and the database of end-member mineral thermodynamic properties from Holland and Powell (2011) (version hp633ver). We considered 14 internally consistent activity-composition models that include biotite, chlorite, chloritoid, cordierite, garnet, ilmenite, mica, staurolite, orthopyroxene and melt from White et al. (2014b, 2014a), epidote from Holland and Powell (2011), feldspar from Holland et al. (2022), clinopyroxene from Green et al. (2007) and spinel from White et al. (2002). The water content was estimated at minimum at the solidus at 8 kbar (*T*-H_2O modelling). We evaluated the consistency between modelled and observed mineral modes with isomodes (vol. %) of plagioclase, biotite and garnet (Duesterhoeft and Lanari, 2020). We further evaluated the influence of intracrystalline deformation affecting the attained *P*–*T* conditions in garnet 'low'- and 'high-strain' domains using the almandine (X_{Alm}), pyrope (X_{Prp}), grossular (X_{Grs}) and spessartine (X_{Spss}) isopleths, considering the EPMA data obtained from garnet-2 displaying the wider and well-developed 'high-strain' domain.

3.4. Multi-mineral isotopic analysis

Garnet Lu–Hf, apatite and zircon U–Pb and mica Rb–Sr isotopic analyses were carried out in situ on a polished thin section at the GeoHistory Facility (John de Laeter Centre, Curtin University). The analytical setup includes a RESOlution 193 nm ArF excimer laser with a Laurin Technic S155 sample cell coupled to an Agilent 7900 quadrupole mass spectrometer for zircon and apatite U–Pb. Garnet Lu–Hf and biotite Rb–Sr analyses were carried out using an Agilent 8900 triple quadrupole spectrometer running in MS/MS mode (Hogmalm et al., 2017; Simpson et al., 2021; Ribeiro et al., 2024). A 'squid' mixing device (Laurin Technic) was used to smooth the pulses of aerosol between the laser and mass spectrometer. Unknowns were bracketed with reference materials to account for instrumental drift and assess accuracy and precision. Laser conditions, gas flow, and mass spectrometer setup are summarised in SM[1] . Garnet Lu–Hf, apatite and zircon U–Pb and biotite Rb–Sr diagrams and dates were calculated with IsoplotR (Vermeesch, 2018), with propagated uncertainties presented as two standard error (2SE). Garnet Lu–Hf and biotite Rb–Sr isochrons are presented in inverse space following Li and Vermeesch (2021). Additional technical details are available in the supplementary material SM[1], and the complete isotopic dataset are presented in SM[3].

Garnet Lu–Hf analyses were carried out in two sessions, in which glass NIST SRM 610 with known ^{176}Lu/^{177}Hf and ^{176}Hf/^{177}Hf composition (Nebel et al., 2009) was employed as primary reference material. Two secondary garnet reference materials (GWA–1 and GWA–2) were further employed to account for laser-induced matrix effects and secondary age checks (Ribeiro et al., 2024). We filtered time-resolved signals using trace element signals (e.g., Y and Zr) to avoid the potential influence of Lu- and Hf-bearing inclusions on ^{176}Hf/^{177}Hf, which has not observed in our dataset (Fig. S1). In session one, GWA–1 yielded a matrix-uncorrected inverse isochron date of 1323 ± 22 Ma (N = 33, MSWD = 0.9), indicating an offset of ~4.4 % compared to the isotope dilution Lu–Hf reference age (1267 ± 3 Ma; Ribeiro et al., 2024). After applying this correction factor (1.044) to the ^{176}Lu/^{176}Hf ratios following Ribeiro et al. (2024), GWA–1 and GWA–2 yielded matrix corrected inverse isochron dates of 1269 ± 22 Ma (N = 33, MSWD = 0.8) and 948 ± 26 Ma (N = 30, MSWD = 0.6), respectively, consistent with reference ages (Ribeiro et al., 2024). In session two, GWA–1 yielded a matrix-uncorrected inverse isochron date of 1301 ± 15 Ma (N = 27, MSWD = 1.4), indicating an offset of ~2.7 % compared to the isotope dilution Lu–Hf reference age. After applying this correction factor (1.027) to the ^{176}Lu/^{176}Hf ratios, GWA–1 and GWA–2 yielded matrix corrected inverse isochron dates of 1267 ± 15 Ma (N = 27, MSWD = 1.3) and 940 ± 27 Ma (N = 29, MSWD = 1.3), respectively, in agreement with reference ages.

Zircon 91,500 (Wiedenbeck et al., 1995) and Mount McClure apatite (Schoene and Bowring, 2006) were employed as primary reference materials for zircon and apatite U–Pb analyses, respectively. Zircon GJ-1 (Jackson et al., 2004) and Plešovice (Slama et al., 2008) were employed as secondary reference materials and treated as unknowns, yielding weighted ^{206}Pb/^{238}U mean dates of 609 ± 3 Ma (N = 24, MSWD = 1.1) and 306 ± 2 Ma (N = 22, MSWD = 1.1), respectively, in agreement with reference ages. Madagascar (Thomson et al., 2012), Duluth-FC1 (Schmitz et al., 2003; Thomson et al., 2012) and Otter Lake (Barfod et al., 2005; Chew et al., 2011) apatite were employed as secondary reference materials and treated as unknowns. Madagascar apatite yielded a lower intercept date of 467 ± 2 Ma (N = 26, MSWD = 0.8) on the Tera–Wasserburg diagram. The Duluth-FC1 and Otter Lake apatite yielded lower intercept dates of 1094 ± 14 Ma (N = 26, MSWD = 0.7) and 875 ± 10 Ma (N = 1.5, MSWD = 1.5), respectively.

The ^{87}Rb/^{86}Sr and ^{87}Sr/^{86}Sr ratios were drift-corrected and calibrated against NIST SRM 610 (Woodhead and Hergt, 2001). Matrix correction of drift–corrected ^{87}Rb/^{86}Sr was applied to biotite analyses using a fractionation factor obtained from a pressed powder tablet of phlogopite Mica-Mg that was analysed interspersed with the unknowns, assuming a crystallization age of 519.4 ± 6.5 Ma and ^{87}Sr/^{86}Sr$_i$ of 0.72607 ± 0.00070 (Hogmalm et al., 2017). Analyses of unknowns were bracketed with in-house biotite reference material CK001 (422 ± 6 Ma; Kirkland et al., 2007) and Mica-Fe (303 ± 2 Ma; Rösel and Zack, 2022), which yielded isochron dates of 418 ± 17 Ma (N = 30, MSWD = 0.8) and 300 ± 6 Ma (N = 30, MSWD = 0.2), respectively.

4. Results

4.1. Garnet microstructures

We observed deformation-related microstructures on four garnet grains through EBSD mapping (Fig. 2). Garnet-1 displays a well-defined low-angle boundary (LAB) up to 1.5° with slight crystallographic misorientation (Fig. 2A). A relatively 'high-strain' (i.e., comparatively more deformed) domain limited by a 2° boundary is present in the lower right edge (Fig. 2A and B). This domain accumulated up to 5° misorientation and displays well-defined LABs forming a small dislocation network (Fig. 2B). Garnet-1 displays LABs < 1° with three main orientations (b_1–b_3, Fig. 2B), defining elongate polygonal subgrains of variable sizes (~20–500 μm). These subgrains are characterised by a density of tilt boundaries given by the geometrically necessary density (GND) of ~$3 \cdot 10^{13}$ m^{-2} with a maximum misorientation angle of 10°. Crystallographic axes are dispersed along small circles displaying complexity with divergent clusters (Fig. S4).

Garnet-2 is dominated by a 'low-strain' domain displaying LABs up to 0.5°, with negligible textural misorientation, crosscut by late-stage fractures (Figs. 2C). The lower-right corner displays a large 'high-strain' domain bounded by high-angle boundaries up to 13°, accumulating ~15° relative misorientation to the garnet core (Fig. 2C and D). The 'high-strain' domain is characterised by a dislocation network with elevated GND of ~$1.5 \cdot 10^{14}$ m^{-2} compared to garnet-1. The crystallographic axes of the 'high-strain' domain are dispersed along small circles with divergent clusters (Fig. S2).

Garnet-3 is microstructurally dominated by a wide 'low-strain' domain bounded by a LAB up to 0.8° with negligible misorientation (Fig. 2E and F). The 'high-strain' domain located in the top right edge is bounded by a high-angle boundary (4° misorientation), accumulating up to 35° misorientation compared to the 'low-strain' domain (garnet-3 core). Such 'high-strain' domain displays a dislocation network with GND >$2.0 \cdot 10^{14}$ m^{-2}, similar to the 'high-strain' microstructures observed in garnet-2 (Fig. 3D).

Similar to the other garnet grains, garnet-4 is also dominated by wide 'low-strain' domains bounded by curved to straight LABs (up to 1.3°), accumulating negligible misorientation across the grain (up to 2°), crosscut by late planar fractures (Fig. 2G). The lower corner displays an asymmetric 'high-strain' domain accumulating up to 5° misorientation relative to the 'low-strain' domain (Fig. 2H), characterised by dislocation network with GND of ~$1.5 \cdot 10^{14}$ m^{-2}.

4.2. Garnet major element chemistry

Based on the array of microstructures, we selected garnet-1 and -2 to evaluate the effect of garnet subgrain recrystallisation and intracrystalline deformation (associated with the formation of dislocation networks) on major element chemistry variability (Fig. 3A and B).

X-ray elemental maps of garnet-1 indicate homogeneous composition across the subgrain domain (Fig. 3A and C), with a narrow rim defined by a sharp Ca increase and Mg decrease (Fig. 3C). Minor Ca enrichment occurs along LABs connected to the mylonitic matrix and around quartz inclusions (Fig. 3C), which probably facilitated communication with the mylonitic matrix during retrograde metamorphism. Garnet-1 has homogeneous Fe and Mn composition across the subgrain and high-strain domain, lacking signs of microstructurally-controlled resorption.

Despite displaying similar chemical characteristics to garnet-1, the X-ray elemental maps from garnet-2 indicate an anhedral faint core with slightly higher Ca content compared to adjacent 'low-strain' domains (Fig. 3D), and a narrow rim defined by a sharp Ca increase. We note higher Ca and lower Mg concentration within the 'high-strain' dislocation network domain (Fig. 3D), whilst maintaining a homogeneous Fe and Mn composition lacking signs of resorption.

4.3. Trace element distribution

Complementary to major element analysis, we selected garnet-3 and -4 displaying a range of microstructures to evaluate the impact of intracrystalline deformation on garnet trace element mobility.

Garnet-3 display a clear microstructural distinction between the 'low-strain' (garnet core with higher P, lower Ca concentration) and 'high-strain' (lower P, higher Ca concentration) domains, containing a well-developed dislocation network (Fig. 4A and B). The 'low-strain' garnet core is characterised by mostly homogeneous trace element, including P, Sc, Ti, Y, Zr, Sm, Lu and Hf, although subtle variations in association with LABs (decrease in Sc, Ti, V, Zr) and fractures (increase in Zr and Hf) are observable (Fig. 4B). The boundary between the 'low-'

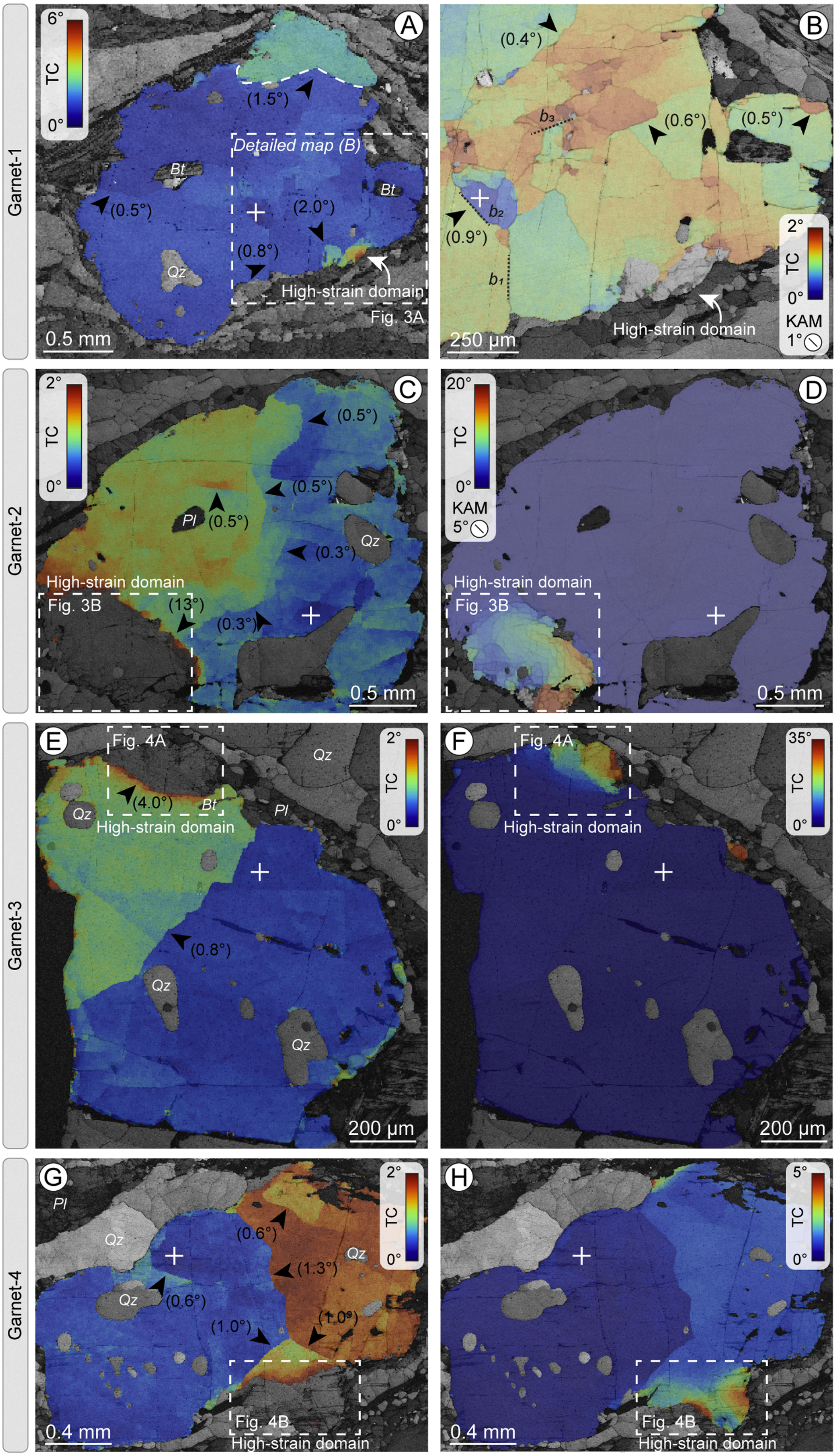

Fig. 2. Textural component maps (TC; relative to the white-cross) highlighting the misorientation across the garnet porphyroclasts (A–B, garnet-1; D–E, garnet–2; E–F, garnet-3; G–H, garnet-4). KAM stands for Kernel average misorientation. Detailed microstructural maps from the high-strain domains are presented in Figs. 3 and 4 along with chemical maps (major and trace elements).

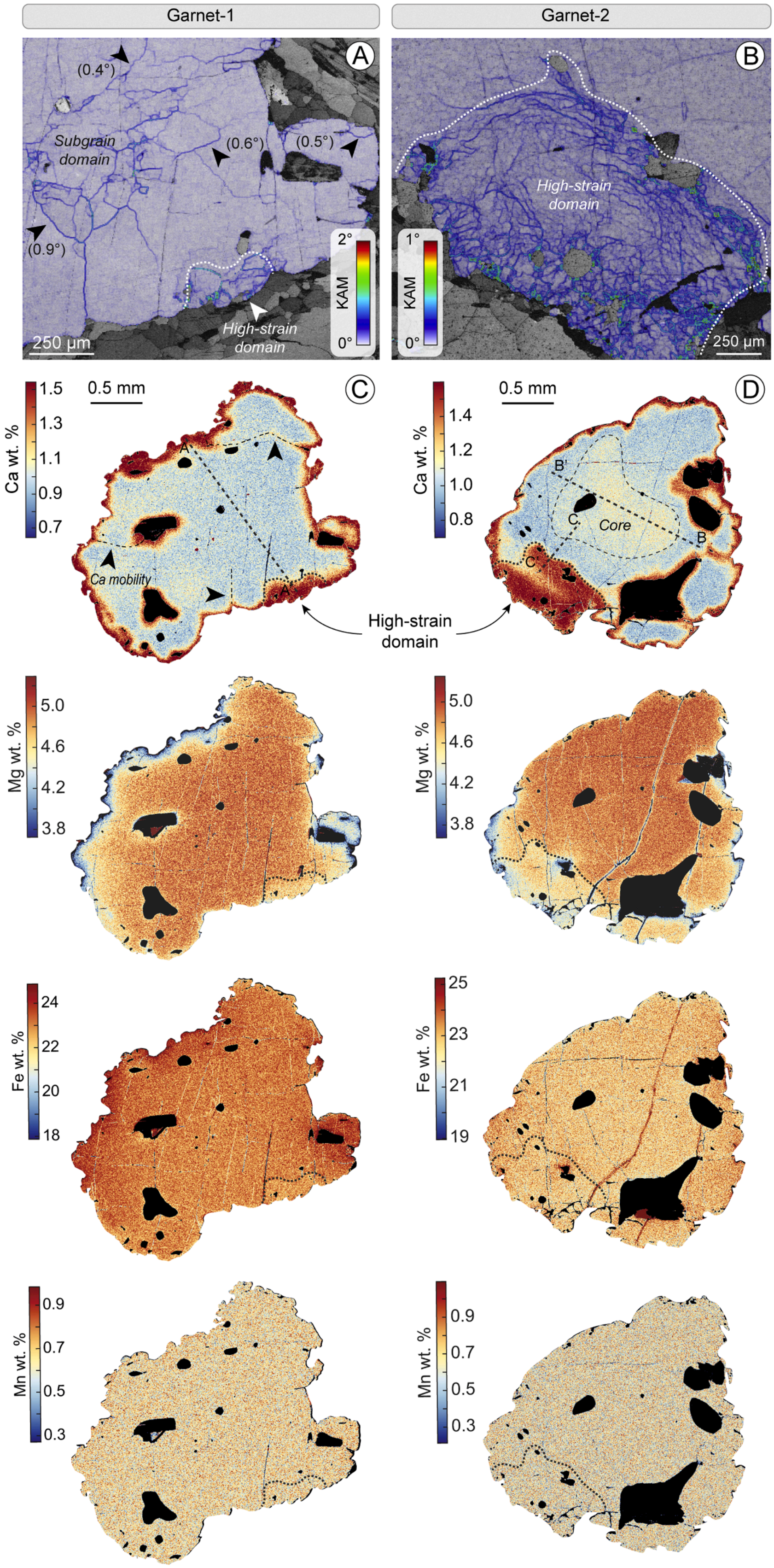

Fig. 3. Garnet Kernel average misorientation (A, B) and X-ray elemental maps (C, D) garnet-1 and -2. Chemical and microstructural profiles A–A', B–B', C–C' are shown in Fig. 8 (see discussion).

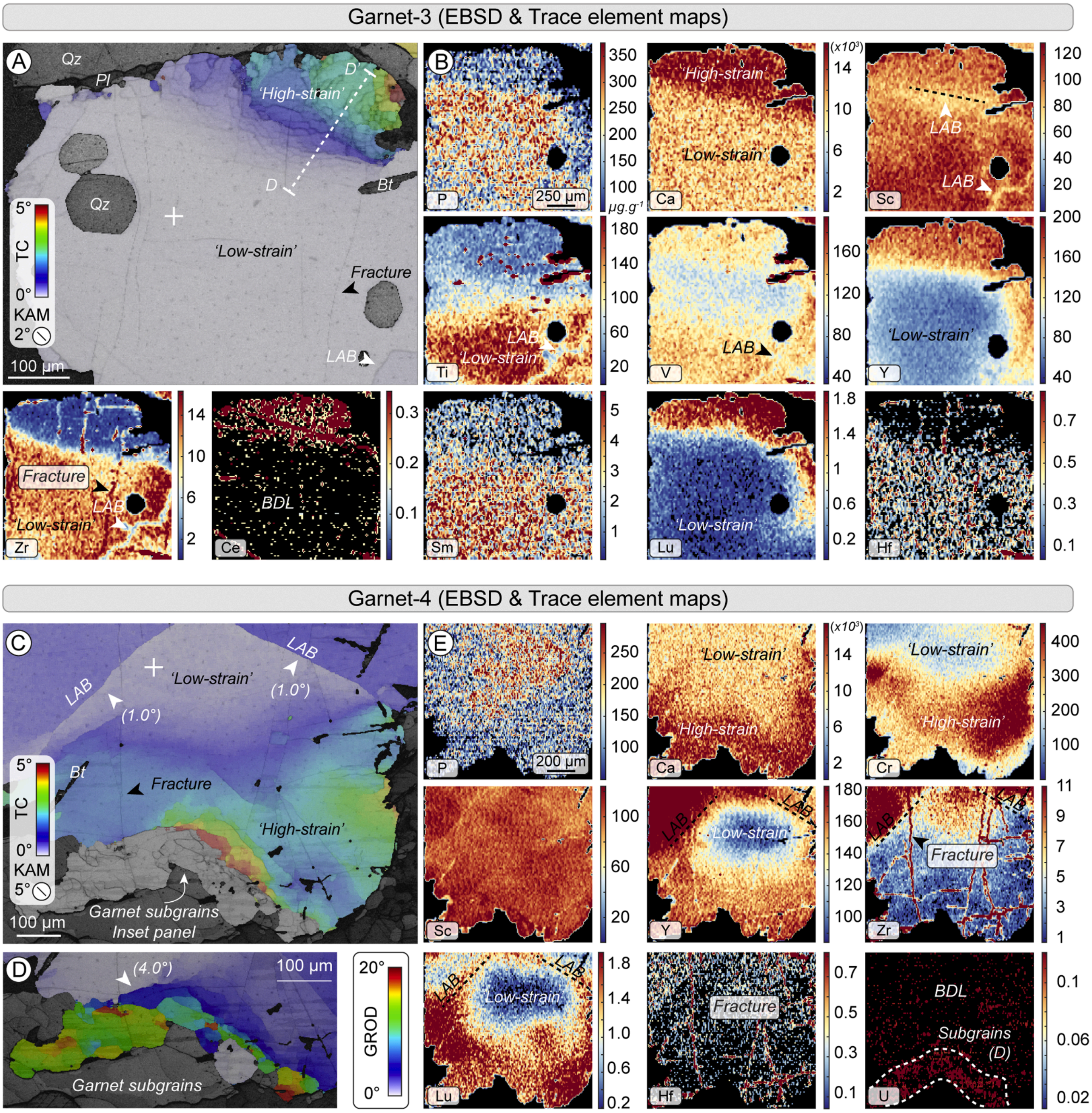

Fig. 4. Composite microstructural maps with overlayered textural component (TC; relative to the white-cross) and Kernel average misorientations (KAM) (A, garnet-3; C, garnet-4), grain reference orientation deviation (GROD) of garnet subgrains (D), and associated trace element maps (B, garnet-3; E, garnet-4). Misorientation and trace element profiles (D–D') are presented in Fig. 9 (see discussion). Trace element maps and scale-bars display element concentration in µg.g^{-1}.

to 'high-strain' domain is defined by a sharp trace element transition (Fig. 4B), decreasing in Ti, Zr, Sm and Hf whilst increasing Y, Ce and Lu concentration within the 'high-strain' dislocation network domain.

Garnet-4 has a complex microstructural setting with numerous planar LABs (up to 1°), and sectored 'high-strain' domains containing a dislocation network around and within the garnet subgrain domain (Fig. 4C and D). In addition to the trace element characteristics described for garnet-3, we note an increase in Cr and U concentration within the 'high-strain' and subgrain domains, respectively, compared to the 'low-strain' domains (Fig. 4E). Low-angle boundaries apparently control Y, Zr and Lu distribution (Fig. 4E).

4.4. *Phase equilibrium modelling*

The interpreted peak metamorphic assemblage (Bt–Gt–Ilm–Afs–Pl–Qz–Sil–Melt) is predicted to be stable between ~790–840 °C and ~8.0–10.5 kbar (Fig. 5A). Isomodes of plagioclase, biotite and garnet overlap with the interpreted stability field (Fig. 5A), matching with the observed abundance of those phases in the sample (Fig. 1A and S2). Modelled garnet compositions within the stability field are similar to measured compositions in garnet-1 and -2 (Fig. 5B), demonstrating initial garnet crystallization under high-*T* conditions.

4.5. *Garnet Lu–Hf isotopes*

We pioneered a new in situ Lu–Hf technique via triple quadrupole

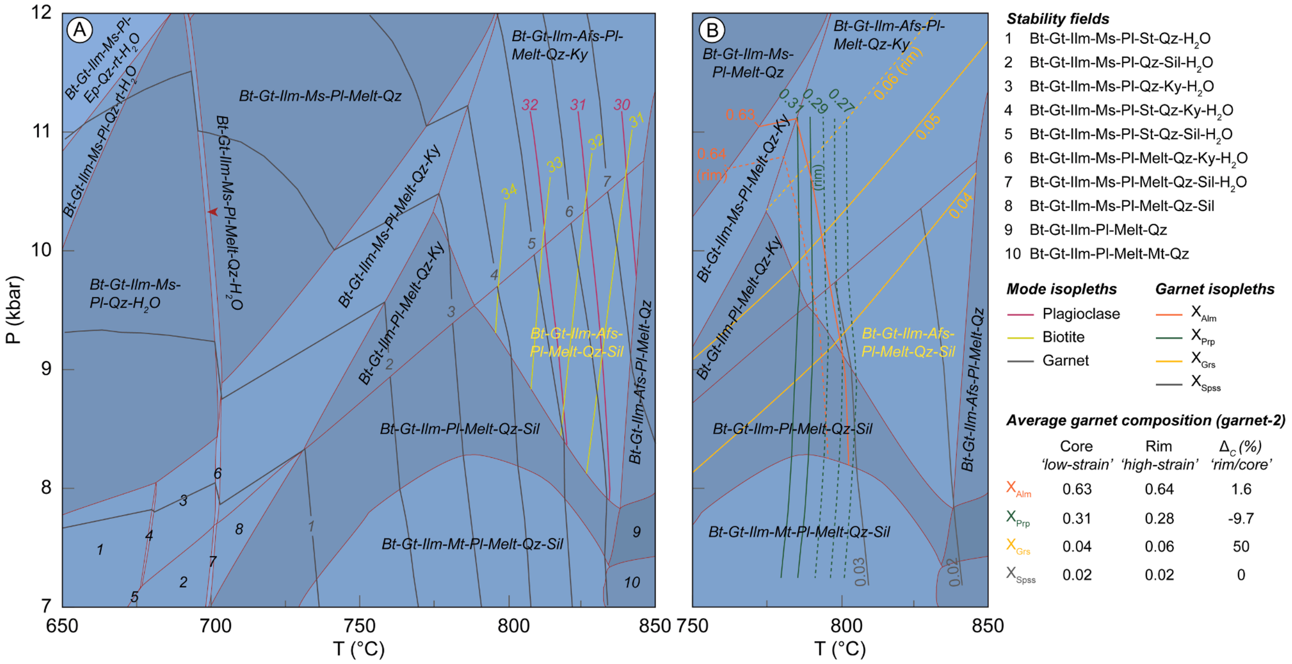

Fig. 5. Isochemical diagrams from the mylonitic paragneiss (R3–7A) contoured by the mode isopleths of plagioclase, biotite and garnet (vol. %; A), and the garnet end-member isopleths (B). The mineral assemblage highlighted in yellow (Bt-Gt-Ilm-Afs-Pl-Melt-Qz-Sil) represents the equilibrium assemblage from the mylonitic paragneiss. The average garnet composition refers to the 'low'- and 'high-strain' domains from garnet-2. Mineral abbreviations follow Whitney and Evans (2010).

ICP-MS/MS to explore the effect of deformation on garnet isotopes. This technique allows, for the first time, the characterisation of 'low'- and 'high-strain' domains with sensible textural control. These data reinforce the depleted radiogenic ^{176}Hf* content (overall <0.1 µg.g^{-1}) in 'high-strain' compared to 'low-strain' domains (overall ~0.1–0.4 µg.g^{-1}; Fig. 6A), as indicated by the trace element distribution in garnet-3 (Fig. 4). The ^{176}Hf* depletion in 'high-strain' domains led to a higher analytical uncertainty in the ^{176}Lu/^{176}Hf and ^{177}Hf/^{177}Hf ratios (Fig. 6B).

When treated separately based on the microstructural and geochemical features, the 'low-strain' domain dataset defines a robust inverse isochron with variable ^{176}Lu/^{176}Hf ratios up to ~50 and ^{177}Hf/^{176}Hf ratios down to ~1.0, yielding an isochron date of 612 ± 20 Ma (MSWD = 1.1, N = 162; Fig. 6C). Conversely, the 'high-strain' domain dataset is characterised by a narrower spread in ^{176}Lu/^{176}Hf (up to ~15) and relatively high ^{177}Hf/^{176}Hf ratios, yielding an isochron date of 522 ± 137 Ma (Fig. 6D).

4.6. *Multi-mineral geochronology*

Additional geochronometers including apatite and zircon U–Pb and biotite Rb–Sr provide a framework for understanding the garnet Lu–Hf dates. Subhedral to anhedral apatite inclusions in garnet define a mixing trend between radiogenic and common-Pb components in the Tera–Wasserburg diagram yielding a lower intercept date of 611 ± 5 Ma (N = 24, MSWD = 0.7; Fig. 7A). Anhedral and sub-rounded zircon grains embedded in the mylonitic matrix display mostly a homogeneous dark response in backscatter imaging, and sector zoning in cathodoluminescence lacks textural evidence of recrystallised rims (Fig. 7B, inset). Zircon grains with average Th/U of 0.37 define a discordia array yielding upper and lower intercept dates of 2463 ± 21 and 521 ± 15 Ma (N = 10, MSWD = 1.9). The Paleoproterozoic upper intercept date is inferred to reflect the timing of protolith's crystallisation (Juiz de Fora Complex; e.g., Araujo et al., 2021), whereas the lower intercept is interpreted to reflect Pb-loss related to a Cambrian thermal event. The apatite and zircon lower intercept dates are, respectively, consistent with the with the 'low'- and 'high-strain' garnet Lu–Hf isochron and model dates.

Biotite defining spaced mylonitic foliation and pressure shadows and included in garnet porphyroclasts were targeted for in situ Rb–Sr analysis. Regardless of the microstructural site, the biotite Rb–Sr data defines a well-constrained inverse isochron date of 489 ± 3 Ma (N = 85, MSWD = 0.8), with an initial ^{87}Sr/^{86}Sr of 0.730 ± 0.006 (Fig. 6C).

5. Discussion

5.1. *Linking deformation and element mobility*

Garnet is a reactive mineral to metamorphic processes, preserving growth mechanisms in its shape, and major and trace element zoning (e.g., Rubatto et al., 2020). The studied garnet grains herein are euhedral to subhedral displaying homogeneous major and trace element distribution in the 'low-strain' core, lacking signs of resorption processes often highlighted by complex major and trace element patterns (de Béthune et al., 1975; Rubatto et al., 2020). The homogeneity in major elements, slow diffusion trace elements (e.g., P and Y) and transition metals (e.g., Sc, V, Cr) is suggestive of a pre-kinematic single garnet growth stage under high-grade conditions (~790–840 °C and ~8.0–10.5 kbar) as constrained by the phase equilibrium modelling (Fig. 5). Such interpretation is consistent with quartz crystallographic data (Fig. 1D), indicating high-T and strain conditions, and with P–T estimates for the regional metamorphic conditions for the central Ribeira Belt (850 ± 50 °C, 8.0 ± 1.0 kbar) during the Neoproterozoic (c. 610 Ma) (Bento dos Santos et al., 2011).

Under high-T and strain conditions, garnet is expected to undergo intracrystalline deformation. The observed garnet microstructures, including low-angle subgrain boundaries and dislocation networks are consistent with intracrystalline deformation via dislocation creep (Prior et al., 2000, 2002). Such microstructures are overprinted by fracturing likely associated with shear zone exhumation below amphibolite facies (e.g., Voegelé et al., 1998), indicating that microplasticity was not triggered by brittle deformation. Most trace elements (REE–Y–Ti) are unaffected by subsequent brittle deformation (except Zr and Hf; Fig. 4B, E), suggesting a selective replacement process rather than crack-seal

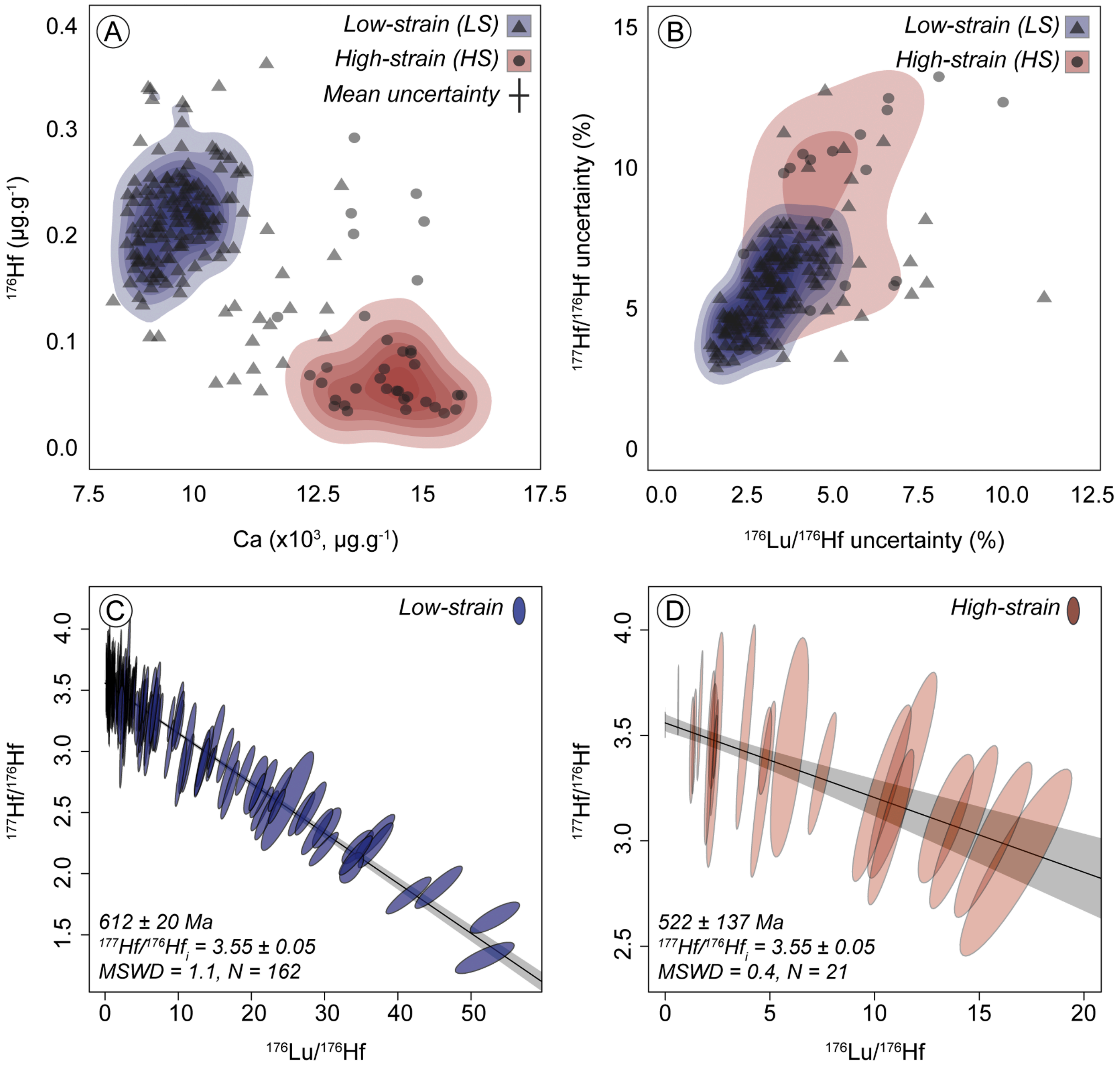

Fig. 6. In situ Lu–Hf isotopic data from the low- and high-strain garnet domains. Scatterplot diagrams of Ca vs. ^{176}Hf* content (B) and the isotopic uncertainties of the ^{176}Lu/^{176}Hf and ^{177}Hf/^{176}Hf ratios from low- and high-strain domains. The Lu–Hf isochron dates of the low-strain (C) and high-strain (D) domains are presented in the inverse space following Li and Vermeesch (2021), with uncertainties stated at 2SE. The isochrons were anchored to an initial ^{177}Hf/^{176}Hf composition of 3.55 ± 0.05 spanning the entire range of initial ^{177}Hf/^{176}Hf ratios of the terrestrial reservoir (Spencer et al., 2019). The Ca vs. ^{176}Hf* scatterplot highlights the greater degree of radiogenic ^{176}Hf* loss in response to the diffusive role of dislocation networks in high-strain garnet domains. Such isotopic loss leads to an increase in the Lu–Hf analytical uncertainty, which is reflected in the greater uncertainty in the isochron dates. The red and blue coloured-domains in the scatterplot diagrams represent statistical density contours (95 % confidence) calculated in RStudio.

mechanisms (e.g., Rubatto et al., 2020).

Although chemical gradients on deformed garnet have been interpreted to reflect chemical segregation induced by dislocation creep, the relationship between diffusional processes and recrystallisation mechanisms remains underexplored (e.g., Chapman et al., 2019). We approach this problem by using the grain reference orientation deviation angle (GROD) to display the relative misorientation of specific textural domains (i.e., ‘low’- and ‘high-strain’) from the grain average orientation. We also consider the Ca content in terms of grossular end-member (X_{Grs}) profiles across the garnet microstructures. Profile A–A’ across subgrains shows a homogeneous composition despite widespread LABs highlighted by small steps in the misorientation profile (Fig. 8A). A sharp X_{Grs} increase is observed in the garnet rim within ‘low’- and ‘high-strain’ domains. Thus, we infer that garnet subgrain formation in response to dislocation creep under high-T conditions does not cause significant intragrain chemical diffusion in major elements. Profile B–B’ transects microstructures varying from relatively ‘low’- to ‘higher strain’ bounded by LAB up to 0.5° (Fig. 8B). The X_{Grs} profile lacks a clear relationship with misorientation.

We also extracted trace element profiles from LA-ICP-MS maps using the transect sampling function in XMapTools (Lanari et al., 2014) to compare with a GROD profile from garnet-3 (Fig. 4A). The ‘low-strain’ garnet core and the ‘high-strain’ dislocation network domains are bounded by a LAB of ∼5°, accumulating intragrain misorientation up to 20° (Fig. 4A). Some trace element profiles such as Lu and Y indicate an increase in concentration with misorientation (Fig. 9A, B), while other

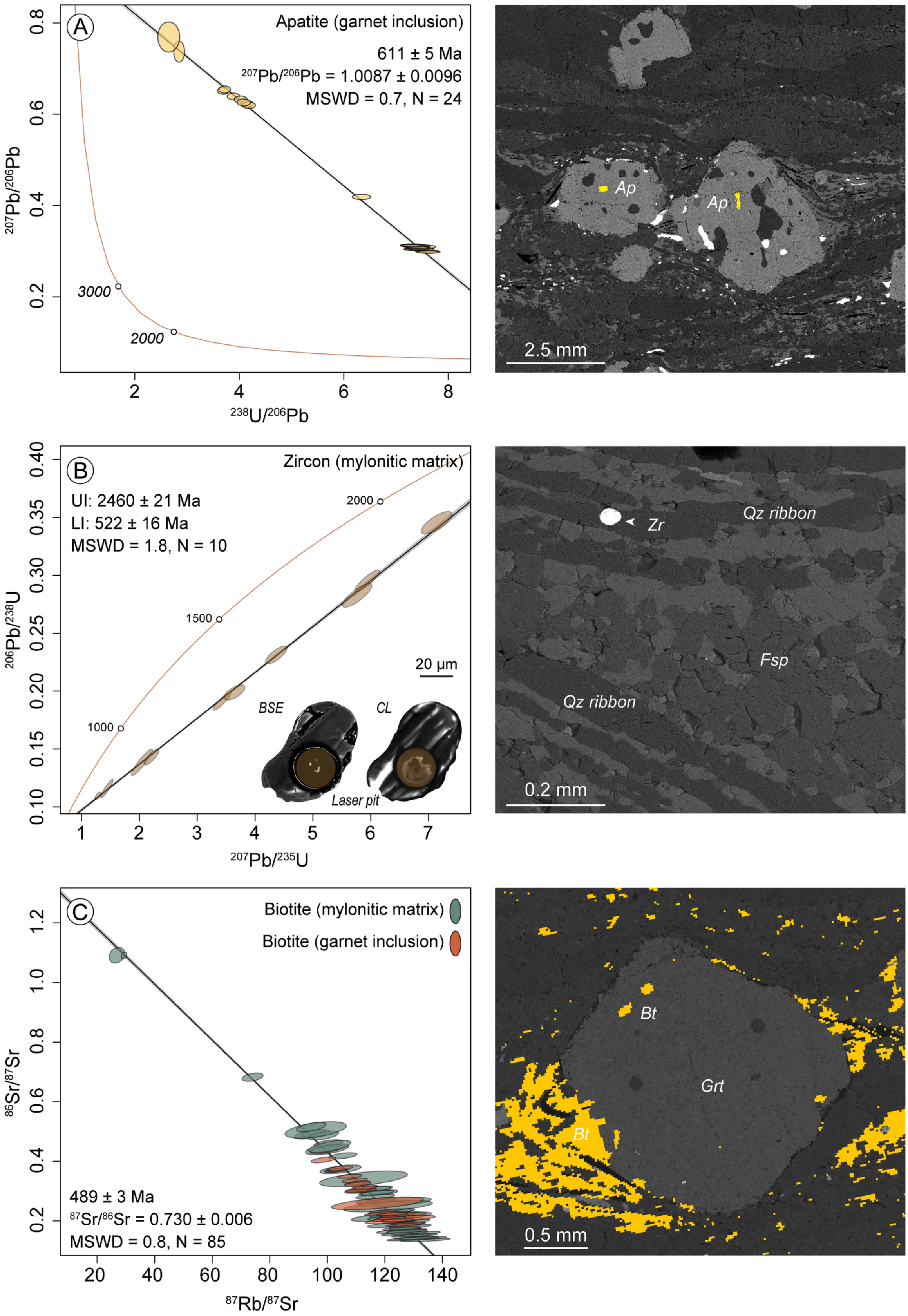

Fig. 7. Apatite (A) and zircon U–Pb (B), and biotite Rb–Sr (C) isotopic data from sample R3–7A. The right panels encompass backscatter electron images of textures of each mineral phase. Note the presence of apatite inclusions in garnet porphyroclasts, small and rounded zircon grains embedded in the mylonitic matrix, and biotite grains present as inclusions in garnet porphyroclasts, in pressure shadows and in the mylonitic matrix. Inset in panel (B) display the zircon backscatter (BSE) and cathodoluminescence (CL) response, with brown circles representing the laser pits from U–Pb analysis. The uncertainties in the isotopic data (ratios and dates) are propagated and stated at 2SE.

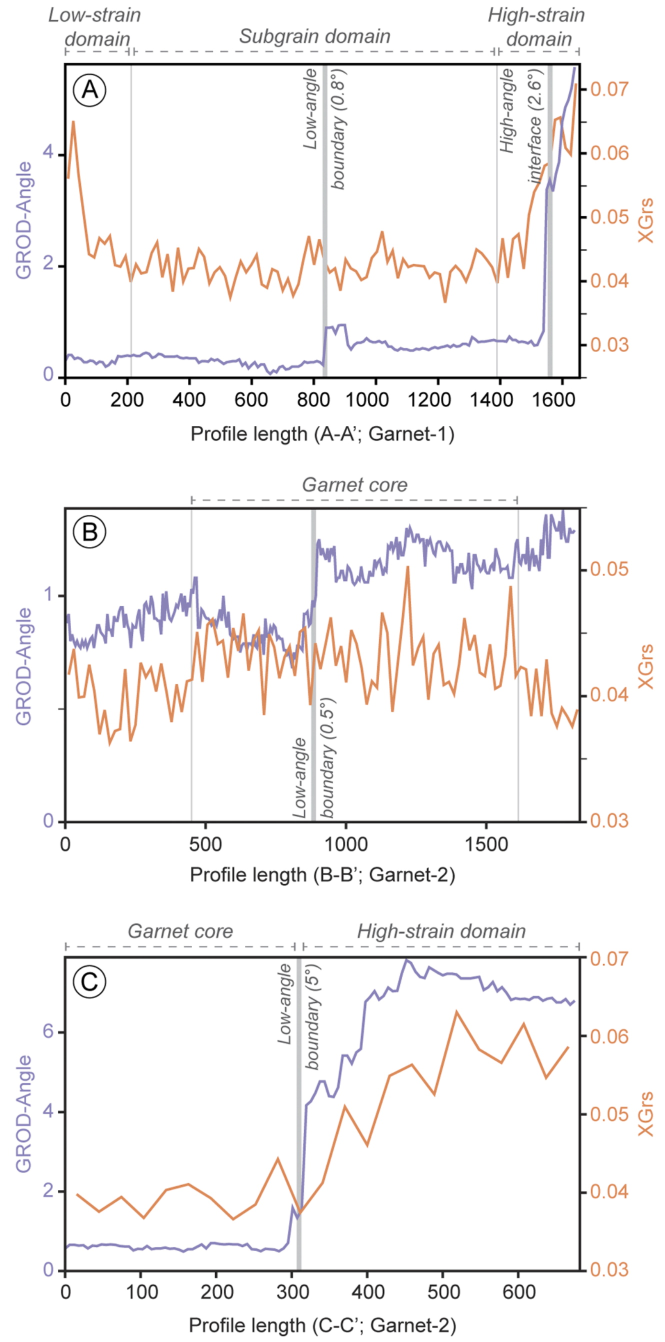

Fig. 8. Cross-correlation between GROD-angle (grain reference orientation deviation) and grossular content (X_{Grs}) across profiles A–A' (A), B–B' (B) and C–C' (C). Chemical profiles were processed and extracted using the transect sampling function in XMapTools (Lanari et al., 2014), and the GROD-Angle profiles were extracted from the EBSD maps using the AZtecCrystal software.

trace elements like Zr and Ti become depleted compared to the 'low-strain' garnet core domain. Trace element maps show that the 'low-strain' garnet core displays homogeneously low concentrations of light rare earth elements (LREEs), Lu and Y, and higher P, Ti and Zr concentration compared to the 'high-strain' domains, likely reflecting growth characteristics during regional granulite facies metamorphism (Bento dos Santos et al., 2011).

Modelled Lu and Y diffusion coefficients from representative profiles extracted from garnet-3 (expressed in log*D* [$m^2 \bullet s^{-1}$]; Figs. 9C and D) are consistent with literature diffusion data calculated at ~800 °C and 1 GPa (Carlson, 2012; Bloch et al., 2015; Rubatto et al., 2020), similar to our peak metamorphic estimates. The low concentration of Hf within the 'high-strain' domain (below detection level for trace element mapping via LA-ICP-MS) prevent a comparison of its diffusivity with Lu. We note that the low Zr concentration in 'high-strain' domains with sharp boundaries (Fig. 4B and E, 9B) suggests that the development of a dislocation network occurred during retrograde subsolidus metamorphism (e.g., Hermann and Rubatto, 2009). At lower temperatures, diffusion coefficients are predicted to be slower than our estimates based on the Arrhenius equation. However, the presence of dislocation networks appears to have enhanced trace element diffusion from 'low'- to 'high-strain' garnet domains, resulting in rates comparable to those observed under high-*T* conditions. This suggests that deformation processes likely influenced trace element mobility during retrograde metamorphism.

The relationship between chemistry (major and trace element) and LABs indicates that individual dislocations are unlikely to facilitate significant intragrain chemical diffusion on the grain scale, despite favouring nanoscale element segregation diffusion via fast-diffusivity pathways (pipe diffusion) and/or defect-impurity pair diffusion (Tacchetto et al., 2022; Dubosq et al., 2024). We envisage that the volume of such nanoscale segregation is negligible within the grain-scale chemical system to promote a bulk grain chemical modification. Yet, our findings indicate that major and trace elements are affected by syn-deformation diffusional transport once the dislocation density is sufficient to form a dislocation network (GND $>1.0 \bullet 10^{14}$ m^{-2}). Irrespective of the diffusion mechanism, these processes are only efficient in promoting grain-scale elemental mobility once a dislocation network has formed, creating favourable microstructural domains to enhance metamorphic reactions and chemical zoning (Caddick et al., 2010; Chapman et al., 2019).

5.2. *Intracrystalline deformation and P–T estimates*

Since garnet is a key mineral for estimating the *P*–*T* conditions of metamorphic processes, assessing the influence of intracrystalline deformation on *P*–*T* estimates may prove crucial to evaluate garnet's robustness and reliability as a key petrochronometer. We assessed the reliability of garnet as a petrological tool in high-strain and temperature systems by coupling phase equilibrium modelling and garnet chemistry from 'low'- and 'high-strain' domains from garnet-2.

As discussed previously, the garnet major and trace element data from the 'low-strain' core domains suggest a single garnet growth stage at high-grade conditions (Bento dos Santos et al., 2011). The X_{Spss} and X_{Alm} contents of garnet are mostly invariable between 'low'- and 'high-strain' domains, overlapping with the predicted stability field (Fig. 5B). However, X_{Grs} values (and X_{Prp} to a lesser extent) are variable, being primarily controlled by apparent changes in pressure (Fig. 5B). Elevated X_{Grs} content in the 'high-strain' dislocation network domain is suggestive of a higher pressure up to ~11 kbar, although it is difficult to assess if this truly represents an equilibrium composition as predicted from phase equilibrium modelling (Palin et al., 2016; Yakymchuk, 2017 and references therein). Our modelling suggests that resolvable *P*–*T* estimates from 'low'- and 'high-strain' domains would require an extensive chemical modification enhanced by intracrystalline deformation, which is unlikely achieved by diffusion via fast-diffusivity pathways (pipe diffusion) and/or defect-impurity pair diffusion as previously suggested (Tacchetto et al., 2022; Dubosq et al., 2024). Therefore, despite indicating that dislocation networks facilitate element mobility in 'high-strain' domains, our findings indicate that the attained *P*–*T* conditions inferred from the major element compositions of garnet porphyroblasts can be considered a robust and reliable petrological tool in high-strain and high-*T* conditions as long as deformation-induced element mobility does not lead to dramatic chemical modifications.

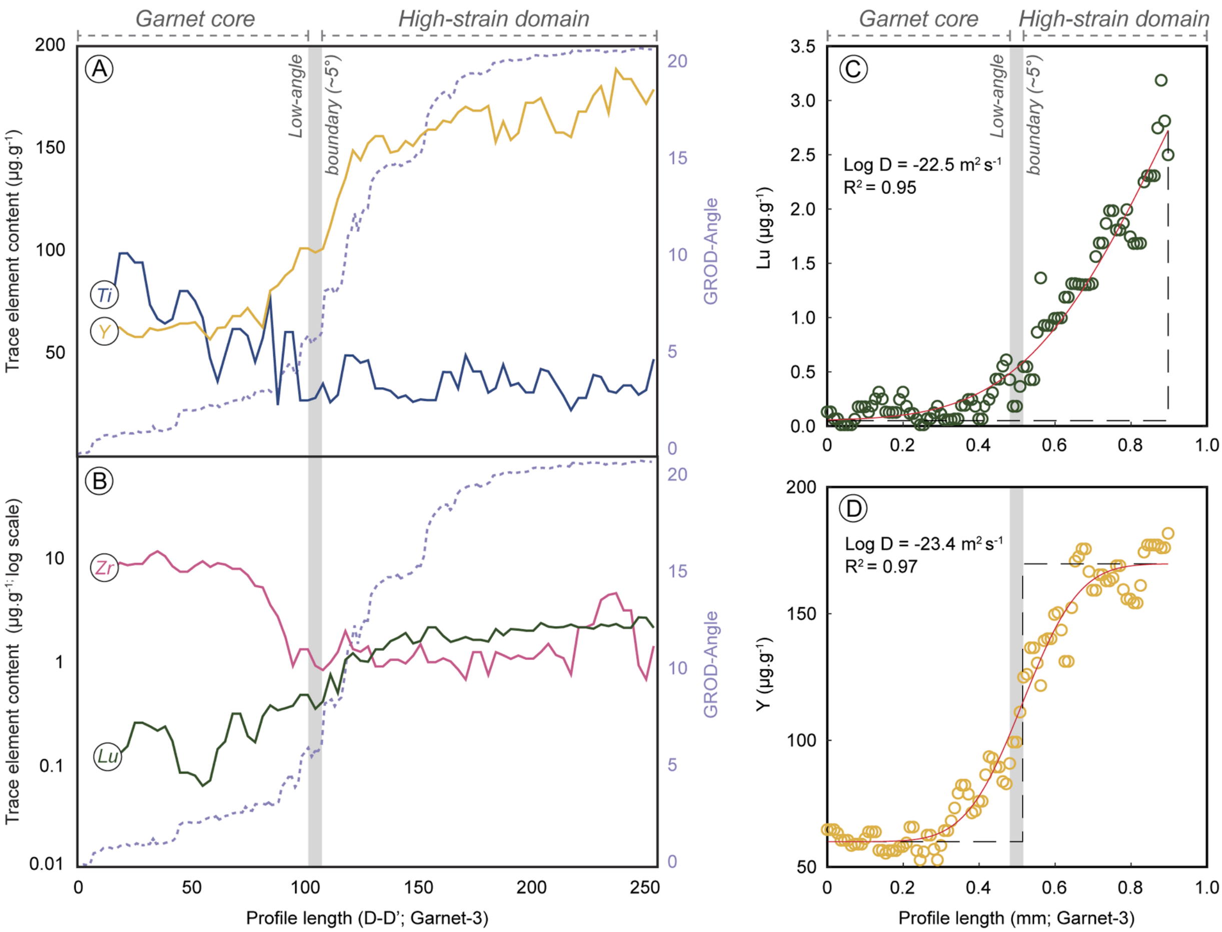

Fig. 9. Cross-correlation between GROD-angle (grain reference orientation deviation) and trace element content (Y, Ti, Zr and Lu) across profiles D–D' from garnet-3 (Fig. 4A, B), and Lu (C) and Y (D) diffusion modelling profiles. Trace element profiles were processed and extracted using the multi-map transect sampling function in XMapTools (Lanari et al., 2014). Diffusion coefficient modelling was carried out using Diffuser (Wu et al., 2022) by applying the Fick's second law for diffusion along one-dimension with a ∼90 Myr period based on the date differences 'low'- and 'high-strain' garnet domains and zircon U–Pb lower intercept date (Fig. 10).

5.3. Intracrystalline influence on Lu–Hf isotopes

The behaviour of Lu–Hf isotopes on garnet has been debated in the literature based on diffusion experiments and natural garnet response (Scherer et al., 2000; Tirone et al., 2005; Smit et al., 2013, 2024; Bloch et al., 2015), which has significant implications for understanding garnet Lu–Hf dates. Irrespective of the preferred model to explain the significance of garnet Lu–Hf dates, it is pivotal to highlight that previous studies employing diffusion experiments and isotopic analysis were carried out on undeformed garnet and with multi-grains isotope dilution techniques. Although applicable to undeformed rocks, such models neglect the influence of intracrystalline deformation features such as dislocation networks promoting element diffusion as shown in this study.

Resolving how intracrystalline deformation affects garnet Lu–Hf dates has traditionally proved challenging due to technical barriers for acquiring isotopic data with sensible spatial resolution using in situ laser ablation techniques. Such limitations were overcome with the development of reaction cell mass spectrometry approaches to minimise interferences (Simpson et al., 2021). Trace element maps and in situ Lu–Hf isotopes show Hf decrease and Lu increase within the 'high-strain' dislocation network compared to 'low-strain' garnet core domains (Fig. 4B and E, 6A). Although isotopic loss during progressive metamorphism is expected for most geochronometers, our data indicate that diffusion of parent and daughter isotopes occurred on dislocation networks. 'Low-strain' garnet core displaying undisturbed Lu–Hf isotopes yields a robust isochron date of 612 ± 20 Ma (Fig. 6C), consistent with U–Pb dates from apatite inclusion in garnet porphyroclasts (611 ± 5 Ma; Fig. 7A, 10). These dates constrain the timing of prograde garnet growth during regional high-T metamorphism prior to ductile shearing in the APSZ (Bento dos Santos et al., 2011; Giraldo et al., 2019). Conversely, the Lu–Hf data from 'high-strain' dislocation networks yield an apparent younger isochron date of 522 ± 137 Ma (Fig. 6D), with larger analytical uncertainty reflecting the pronounced ^{176}Hf* loss enhanced by the dislocation network (Fig. 6B). To overcome the large uncertainty from the isochron date, we calculated model Lu–Hf model dates from 'low'- and 'high-strain' domains using an anchored approach to initial ^{177}Hf/^{176}Hf ratio of 3.55 ± 0.05, which span the entire range of initial ^{177}Hf/^{176}Hf ratios of the terrestrial reservoir (Spencer et al., 2019). Model Lu–Hf dates from 'low'- and 'high-strain' domains define two distinct normal distributions ($p << 0.05$; t-Test with similar variance) with mean model dates of 610 ± 3 Ma and 520 Ma ± 7 Ma (Fig. 10), respectively. Such model dates, combined with distinct microstructural and chemical characteristics, argue for a Cambrian ductile shearing deformation in the APSZ (Fig. 10). This interpretation is supported by the thermal reset of sector-zoned Paleoproterozoic zircon grains in the mylonitic matrix at 522 Ma ± 16 Ms (Fig. 7B, 10). Biotite Rb–Sr date constrains the cooling of the APSZ at 489 ± 3 Ma at greenschist facies conditions.

Our findings demonstrate for the first time that syn-kinematic intracrystalline deformation facilitates garnet recrystallisation inducing isotopic resetting of 'high-strain' domains once a dislocation network is developed, similar to the observed relationship between intracrystalline deformation and U–Pb–trace element mobility in

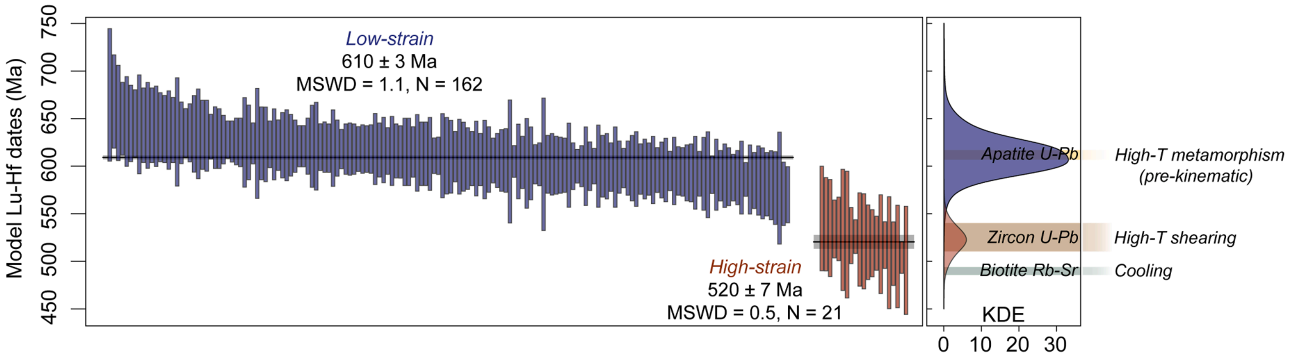

Fig. 10. Weighted mean model Lu–Hf garnet dates from 'low-' and 'high-strain' domains, with Kernel density estimates representing each population on the right inset. Model ages were calculated in IsoplotR (Vermeesch, 2018) using an anchored approach to initial ^{177}Hf/^{176}Hf ratio of 3.55 ± 0.05, which span the entire range of initial ^{177}Hf/^{176}Hf ratios of the terrestrial reservoir (Spencer et al., 2019). The uncertainties in the isotopic data are stated at 2SE, and the model date for each spot analysis is available in SM^3.

deformed zircon (Reddy et al., 2006; Piazolo et al., 2016). Our results suggest that Lu gain coupled to Hf loss induced by dislocation network domains may yield younger dates relative to the timing of prograde garnet growth (Fig. 10). Based on the variation in Sm and U concentration within the 'low'- and 'high-strain' domains (Figs. 4B and E), we envisage that garnet recrystallisation could disturb the Sm–Nd and U–Pb geochronometers. Although in situ garnet U–Pb geochronology has gained relevance (e.g., Bartoli et al., 2024), we note that in situ garnet Sm–Nd via LA-ICP-MS is not yet a developed technique. Future research focused on such techniques could address the impact of garnet deformation/recrystallisation on other geochronometers in addition to Lu–Hf.

6. Conclusion

We demonstrate that garnet porphyroclasts from a high-*T* mylonitic paragneiss undergo intracrystalline deformation via dislocation creep resulting in LABs. Furthermore, our results indicate that individual and disconnected LABs do not promote bulk element mobility on the grain-scale, thus maintaining deformed garnet's geochemical integrity. However, the geochemistry of 'high-strain' garnet is compromised once microstructural domains have accumulated sufficient deformation to form a dislocation network of LABs, promoting diffusion through fast-pathways for major and trace elements. Nevertheless, the *P*–*T* estimates derived from 'low'- and 'high-strain' overlap within uncertainties, implying that even highly deformed garnet porphyroclasts under high-strain and temperature conditions can be reliable to estimate garnet growth. Dislocation networks play a key role in facilitating diffusive loss of Hf and Lu grain, affecting a widely used metamorphic geochronometer and allowing 'high-strain' domains to record the timing of ductile deformation under high-*T* conditions.

CRediT authorship contribution statement

B.V. Ribeiro: Writing – original draft, Visualization, Methodology, Investigation, Formal analysis, Conceptualization. **C.L. Kirkland:** Writing – review & editing, Validation, Investigation, Conceptualization. **M.A. Finch:** Writing – review & editing, Validation, Investigation, Conceptualization. **C. Yakymchuk:** Writing – review & editing, Validation, Formal analysis, Conceptualization. **S.M. Reddy:** Writing – review & editing, Validation, Conceptualization. **F.M. Faleiros:** Writing – review & editing, Validation, Formal analysis, Conceptualization. **K. Goemann:** Writing – review & editing, Validation, Investigation, Formal analysis. **I. Belousov:** Writing – review & editing, Validation, Formal analysis.

Declaration of competing interest

The authors declare that they have no known competing financial interests or personal relationships that could have appeared to influence the work reported in this paper.

Acknowledgements

This research was supported by the Timescales of Mineral Systems Group. The authors thank Tim Johnson, Kyle Larson and Margo Odlum for insightful comments in an earlier draft. Research in the John de Laeter Centre GeoHistory Facility is enabled by AuScope (auscope.org.au) and the Australian Government via the National Collaborative Research Infrastructure Strategy (NCRIS). This research was undertaken using the Tescan Clara FESEM (ARC LE190100176). MF acknowledges funding from the Australian Research Council (DE240100654). We are thankful for supportive and constructive comments from Ethan Baxter, an anonymous reviewer and the editor Alex Webb. BVR thanks Michael Hartnady and Janne Liebmann for constructive discussions.

Supplementary materials

Supplementary material associated with this article can be found, in the online version, at doi:10.1016/j.epsl.2025.119271.

Data availability

The complete dataset is available in the supplementary materials.

References

Araujo, L.E.de A.B., Heilbron, M., Teixeira, W., Dussin, I.A., de Morisson Valeriano, C., Bruno, H., Sato, K., Paravidini, G., Castro, M., 2021. Siderian to Rhyacian evolution of the Juiz de Fora Complex: arc fingerprints and correlations within the Minas-Bahia Orogen and the Western Central Africa Belt. Precambrian Res. 359, 106118. https://doi.org/10.1016/j.precamres.2021.106118 v.

Barfod, G.H., Krogstad, E.J., Frei, R., Albarède, F., 2005. Lu-Hf and PbSL geochronology of apatites from proterozoic terranes: a first look at Lu-Hf isotopic closure in metamorphic apatite. Geochim. Cosmochim. Acta 69, 1847–1859. https://doi.org/10.1016/j.gca.2004.09.014 v.

Bartoli, O., Millonig, L.J., Carvalho, B.B., Marschall, H.R., Gerdes, A., 2024. The age of granulite-facies metamorphism in the Ivrea–Verbano zone (NW Italy) determined through *In situ* U–Pb dating of garnet. J. Petrol. 65. https://doi.org/10.1093/petrology/egae083 v.

Baxter, E.F., Caddick, M.J., Dragovic, B., 2017. Garnet: a rock-forming mineral petrochronometer. Rev. Mineral. Geochem. 83, 469–533. https://doi.org/10.2138/rmg.2017.83.15 v.

Baxter, E.F., Scherer, E.E., 2013. Garnet geochronology: timekeeper of tectonometamorphic processes. Elements 9, 433–438. https://doi.org/10.2113/gselements.9.6.433 v.

Bento dos Santos, T.M., Munhá, J.M., Tassinari, C.C.G., Fonseca, P.E., Neto, C.D., 2011. Metamorphic P-T evolution of granulites in the central Ribeira Fold Belt. SE Brazil: Geosci. J. 15, 27–51. https://doi.org/10.1007/s12303-011-0004-1 v.

de Béthune, P., Laduron, D., Bocquet, J., 1975. Diffusion processes in resorbed garnets. Contrib. Mineral. Petrol. 50, 197–204. https://doi.org/10.1007/BF00371039 v.

Bloch, E., Ganguly, J., Hervig, R., Cheng, W., 2015. 176Lu–176Hf geochronology of garnet I: experimental determination of the diffusion kinetics of Lu3+ and Hf4+ in garnet, closure temperatures and geochronological implications. Contrib. Mineral. Petrol. 169, 12. https://doi.org/10.1007/s00410-015-1109-8 v.

Caddick, M.J., Konopásek, J., Thompson, A.B., 2010. Preservation of garnet growth zoning and the duration of prograde metamorphism. J. Petrol. 51, 2327–2347. https://doi.org/10.1093/petrology/egq059 v.

Campanha, G.A.C., Faleiros, F.M., Cabrita, D.I.G, Ribeiro, B.V., Cawood, P.A., 2023. The southern Ribeira Belt in Western Gondwana: a record of a long-lived continental margin and terrane collage. J. South Amer. Earth Sci. 127, 104404. https://doi.org/10.1016/j.jsames.2023.104404 v.

Carlson, W.D., 2012. Rates and mechanism of Y, REE, and Cr diffusion in garnet. Am. Mineral. 97, 1598–1618. https://doi.org/10.2138/am.2012.4108 v.

Cavalcante, C., Lagoeiro, L., Fossen, H., Egydio-silva, M., Morales, F.G., Ferreira, F., Conte, T., 2018. Temperature constraints on microfabric patterns in quartzofeldsphatic mylonites, Ribeira belt (SE Brazil). J. Struct. Geol. https://doi.org/10.1016/j.jsg.2018.07.013.

Chapman, T., Clarke, G.L., Piazolo, S., Robbins, V.A., Trimby, P.W., 2019. Grain-scale dependency of metamorphic reaction on crystal plastic strain. J. Metamorph. Geol. 37, 1021–1036. https://doi.org/10.1111/jmg.12473 v.

Chew, D.M., Sylvester, P.J., Tubrett, M.N., 2011. U-Pb and Th-Pb dating of apatite by LA-ICPMS. Chem. Geol. 280, 200–216. https://doi.org/10.1016/j.chemgeo.2010.11.010 v.

Dubosq, R., Camacho, A., Rogowitz, A., Zhang, S., Gault, B., 2024. Influence of high-strain deformation on major element mobility in garnet: nanoscale evidence from atom probe tomography. J. Metamorph. Geol. https://doi.org/10.1111/jmg.12758.

Dubosq, R., Schneider, D.A., Camacho, A., Gault, B., 2023. Strain hardening induced by crystal plasticity: A new mechanism for brittle failure in garnets. Earth Planet. Sci. Lett. 617, 118273. https://doi.org/10.1016/j.epsl.2023.118273 v.

Duesterhoeft, E., Lanari, P., 2020. Iterative thermodynamic modelling—Part 1: A theoretical scoring technique and a computer program (<scp>Bingo-Antidote</scp>). J. Metamorph. Geol. 38, 527–551. https://doi.org/10.1111/jmg.12538 v.

Faleiros, F.M., Moraes, R., Pavan, M., Campanha, G.A.C., 2016. A new empirical calibration of the quartz c-axis fabric opening-angle deformation thermometer. Tectonophysics 671, 173–182. https://doi.org/10.1016/j.tecto.2016.01.014 v.

Giraldo, S.J., Trouw, R.A.J., Duffles, P., Vinagre, R., Mejia, M.I., Marimon, R.S., 2019. Structural analysis combined with new geothermobarometric and geochronological results of the Além Paraíba shear zone, between Três Rios and Bananal, Ribeira Orogen, SE Brazil. J. South Amer. Earth Sci. 90, 118–136. https://doi.org/10.1016/j.jsames.2018.11.018 v.

Green, E., Holland, T., Powell, R., 2007. An order-disorder model for omphacitic pyroxenes in the system jadeite-diopside-hedenbergite-acmite, with applications to eclogitic rocks. Am. Mineral. 92, 1181–1189. https://doi.org/10.2138/am.2007.2401 v.

Heilbron, M., Valeriano, C.M., Tassinari, C.C.G., Almeida, J., Tupinambá, M., Siga, O., Trouw, R., 2008. Correlation of Neoproterozoic Terranes Between the Ribeira Belt, SE Brazil and Its African Counterpart: Comparative Tectonic Evolution and Open Questions: Geological Society, 294. Special Publications, London, pp. 211–237. https://doi.org/10.1144/SP294.12 v.

Hermann, J., Rubatto, D., 2009. Accessory phase control on the trace element signature of sediment melts in subduction zones. Chem. Geol. 265, 512–526. https://doi.org/10.1016/j.chemgeo.2009.05.018 v.

Hogmalm, K.J., Zack, T., Karlsson, A.K., Sjoqvist, A.S.L., Grabe-Schonberg, D., 2017. In-situ Rb-Sr and K-Ca dating by LA-ICP-MS/MS: an evaluation of N2O and SF6 as reaction gases. J. Anal. At. Spectrom. 32, 305–313 v.

Holland, T.J.B., Green, E.C.R., Powell, R., 2022. A thermodynamic model for feldspars in $KAlSi_3O_8-NaAlSi_3O_8-CaAl_2Si_2O_8$ for mineral equilibrium calculations. J. Metamorph. Geol. 40, 587–600. https://doi.org/10.1111/jmg.12639 v.

Holland, T.J.B., Powell, R., 2011. An improved and extended internally consistent thermodynamic dataset for phases of petrological interest, involving a new equation of state for solids. J. Metamorph. Geol. 29, 333–383 v.

Jackson, S.E., Pearson, N.J., Griffin, W.L., Belousova, E.A., 2004. The application of laser ablation-inductively coupled plasma-mass spectrometry to in situ U–Pb zircon geochronology. Chem. Geol. 211, 47–69 v.

Kavanagh-Lepage, C., Gervais, F., Larson, K., Grazziani, R., Moukhsil, A., 2022. Deformation induced decoupling between U-Pb and trace elements in titanite revealed through petrochronology and study of localized deformation. Geosci. Frontiers, 101496. https://doi.org/10.1016/j.gsf.2022.101496.

Kirkland, C.L., Daly, J.S., Eide, E.A., Whitehouse, M.J., 2007. Tectonic evolution of the Arctic Norwegian caledonides from a texturally- and structurally-constrained multi-isotopic (Ar-Ar, Rb-Sr, Sm-Nd, U-Pb) study. Am. J. Sci. 307, 459–526. https://doi.org/10.2475/02.2007.06 v.

Lanari, P., Vidal, O., De Andrade, V., Dubacq, B., Lewin, E., Grosch, E.G., Schwartz, S., 2014. XMapTools: A MATLAB©-based program for electron microprobe X-ray image processing and geothermobarometry. Comput. Geosci. 62, 227–240. https://doi.org/10.1016/j.cageo.2013.08.010 v.

Li, Y., Vermeesch, P., 2021. Inverse isochron regression for re-Os, K-Ca and other chronometers. Geochronology. https://doi.org/10.5194/gchron-2021-7 vPreprint.

Mori, P.A., Reeves, S., Correia, C.T., Haukka, M., 1999. Development of a fused glass disc XRF facility and comparison with the pressed powder pellet technique at the Instituto de Geociências, São Paulo University. Revista Brasileira de Geociências 29, 441–446. https://doi.org/10.25249/0375-7536.199929441446 v.

Nebel, O., Morel, M.L.A., Vroon, P.Z., 2009. Isotope dilution determinations of Lu, Hf, Zr, Ta and W, and Hf Isotope compositions of NIST SRM 610 and 612 glass wafers. Geostand. Geoanal. Res. 33, 487–499. https://doi.org/10.1111/j.1751-908X.2009.00032.x v.

Odlum, M.L., Levy, D.A., Stockli, D.F., Stockli, L.D., DesOrmeau, J.W., 2022. Deformation and metasomatism recorded by single-grain apatite petrochronology. Geology. https://doi.org/10.1130/G49809.1.

Palin, R.M., Weller, O.M., Waters, D.J., Dyck, B., 2016. Quantifying geological uncertainty in metamorphic phase equilibria modelling; a Monte Carlo assessment and implications for tectonic interpretations. Geosci. Front. 7, 591–607. https://doi.org/10.1016/j.gsf.2015.08.005 v.

Papapavlou, K., Darling, J.R., Storey, C.D., Lightfoot, P.C., Moser, D.E., Lasalle, S., 2017. Dating shear zones with plastically deformed titanite: new insights into the orogenic evolution of the Sudbury impact structure (Ontario, Canada). Precambrian Res. 291, 220–235. https://doi.org/10.1016/j.precamres.2017.01.007 v.

Piazolo, S., La Fontaine, A., Trimby, P., Harley, S., Yang, L., Armstrong, R., Cairney, J.M., 2016. Deformation-induced trace element redistribution in zircon revealed using atom probe tomography. Nat. Commun. 7, 10490. https://doi.org/10.1038/ncomms10490 v.

Prior, D.J., Wheeler, J., Brenker, F.E., Harte, B., Matthews, M., 2000. Crystal plasticity of natural garnet: new microstructural evidence. Geology 28, 1003. https://doi.org/10.1130/0091-7613(2000)28<1003:CPONGN>2.0.CO;2 v.

Prior, D.J., Wheeler, J., Peruzzo, L., Spiess, R., Storey, C., 2002. Some garnet microstructures: an illustration of the potential of orientation maps and misorientation analysis in microstructural studies. J. Struct. Geol. 24, 999–1011. https://doi.org/10.1016/S0191-8141(01)00087-6 v.

Reddy, S.M., Timms, N.E., Pantleon, W., Trimby, P., 2007. Quantitative characterization of plastic deformation of zircon and geological implications. Contrib. Mineral. Petrol. 153, 625–645. https://doi.org/10.1007/s00410-006-0174-4 v.

Reddy, S.M., Timms, N.E., Trimby, P., Kinny, P.D., Buchan, C., Blake, K., 2006. Crystal-plastic deformation of zircon: A defect in the assumption of chemical robustness. Geology 34, 257. https://doi.org/10.1130/G22110.1 v.

Ribeiro, B.V., et al., 2024. Garnet reference materials for. *Situ* Lu-Hf Geochronology: Geostandards and Geoanalytical Research. https://doi.org/10.1111/ggr.12579.

Ribeiro, B.V., Lagoeiro, L., Faleiros, F.M., Hunter, N.J.R., Queiroga, G., Raveggi, M., Cawood, P.A., Finch, M., Campanha, G.A.C., 2020. Strain localization and fluid-assisted deformation in apatite and its influence on trace elements and U–Pb systematics. Earth Planet. Sci. Lett. 545, 116421. https://doi.org/10.1016/j.epsl.2020.116421 v.

Rösel, D., Zack, T., 2022. LA-ICP-MS/MS Single-Spot Rb-Sr Dating. Geostandards and Geoanalytical Research. https://doi.org/10.1111/ggr.12414.

Rubatto, D., Burger, M., Lanari, P., Hattendorf, B., Schwarz, G., Neff, C., Keresztes Schmidt, P., Hermann, J., Vho, A., Günther, D., 2020. Identification of growth mechanisms in metamorphic garnet by high-resolution trace element mapping with LA-ICP-TOFMS. Contrib. Mineral. Petrol. 175, 61. https://doi.org/10.1007/s00410-020-01700-5 v.

Scherer, E.E., Cameron, K.L., Blichert-Toft, J., 2000. Lu–Hf garnet geochronology: closure temperature relative to the Sm–Nd system and the effects of trace mineral inclusions. Geochim. Cosmochim. Acta 64, 3413–3432. https://doi.org/10.1016/S0016-7037(00)00440-3 v.

Schmitz, M.D., Bowring, S.A., Ireland, T.R., 2003. Evaluation of Duluth Complex anorthositic series (AS3) zircon as a U-Pb geochronological standard: new high-precision isotope dilution thermal ionization mass spectrometry results. Geochim. Cosmochim. Acta 67, 3665–3672. https://doi.org/10.1016/S0016-7037(03)00200-X v.

Schoene, B., Bowring, S.A., 2006. U-Pb systematics of the McClure Mountain syenite: thermochronological constraints on the age of the 40Ar/39Ar standard MMhb. Contrib. Mineral. Petrol. 151, 615–630. https://doi.org/10.1007/s00410-006-0077-4 v.

Simpson, A., Gilbert, S., Tamblyn, R., Hand, M., Spandler, C., Gillespie, J., Nixon, A., Glorie, S., 2021. In-situ Lu Hf geochronology of garnet, apatite and xenotime by LA ICP MS/MS. Chem. Geol. 577, 120299. https://doi.org/10.1016/j.chemgeo.2021.120299 v.

Slama, J., Kosler, J., Condon, D.J., Crowley, J.L., Gerdes, A., Hanchar, J.M., Horstwood, M.S.A., Morris, G.A., Nasdala, L., Norberg, N., Schaltegger, U., Schoene, N., Tubrett, M.N., Whitehouse, M.J., 2008. Plesovice zircon - a new natural reference material for U-Pb and Hf isotopic microanalysis. Chem. Geol. 249, 1–35 v.

Smit, M.A., Scherer, E.E., Mezger, K., 2013. Lu–Hf and Sm–Nd garnet geochronology: chronometric closure and implications for dating petrological processes. Earth Planet. Sci. Lett. 381, 222–233. https://doi.org/10.1016/j.epsl.2013.08.046 v.

Smit, M.A., Vrijmoed, J.C., Scherer, E.E., Mezger, K., Kooijman, E., Schmitt-Kielman, M., Tual, L., Guilmette, C., Ratschbacher, L., 2024. Retentiveness of rare earth elements in garnet with implications for garnet Lu-Hf chronology. J. Metamorph. Geol. https://doi.org/10.1111/jmg.12769.

Spencer, C.J., Kirkland, C.L., Roberts, N.M.W., Evans, N.J., Liebmann, J., 2019. Strategies towards robust interpretations of in situ zircon Lu–Hf isotope analyses. Geosci. Front. 11, 843–853. https://doi.org/10.1016/j.gsf.2019.09.004 v.

Storey, C.D., Prior, D.J., 2005. Plastic deformation and recrystallization of garnet: a mechanism to facilitate diffusion creep. J. Petrol. 46, 2593–2613. https://doi.org/10.1093/petrology/egi067 v.

Tacchetto, T., Reddy, S.M., Fougerouse, D., Clark, C., Saxey, D.W., Rickard, W.D.A., 2022. Crystal plasticity enhances trace element mobility in garnet. Geology. https://doi.org/10.1130/G50283.1.

Thomson, S.N., Gehrels, G.E., Ruiz, J., Buchwaldt, R., 2012. Routine low-damage apatite U-Pb dating using laser ablation–multicollector–ICPMS: geochemistry. Geophys. Geosyst. 13 v.

Tirone, M., Ganguly, J., Dohmen, R., Langenhorst, F., Hervig, R., Becker, H.-W., 2005. Rare earth diffusion kinetics in garnet: experimental studies and applications. Geochim. Cosmochim. Acta 69, 2385–2398. https://doi.org/10.1016/j.gca.2004.09.025 v.

Verberne, R., Reddy, S.M., Saxey, D.W., Fougerouse, D., Rickard, W.D.A., Quadir, Z., Evans, N.J., Clark, C., 2022. Dislocations in minerals: fast-diffusion pathways or trace-element traps? Earth Planet. Sci. Lett. 584, 117517. https://doi.org/10.1016/j.epsl.2022.117517 v.

Vermeesch, P., 2018. IsoplotR: A free and open toolbox for geochronology. Geosci. Front. 9, 1479–1493. https://doi.org/10.1016/j.gsf.2018.04.001 v.

Voegelé, V., Cordier, P., Sautter, V., Sharp, T.G., Lardeaux, J.M., Marques, F.O., 1998. Plastic deformation of silicate garnets. Phys. Earth Planet. Inter. 108, 319–338. https://doi.org/10.1016/S0031-9201(98)00111-3 v.

Walters, J.B., 2022. MinPlot: A mineral formula recalculation and plotting program for electron probe microanalysis. Mineralogia 53, 51–66. https://doi.org/10.2478/mipo-2022-0005 v.

Wang, Z., Ji, S., 1999. Deformation of silicate garnets: brittle-ductile transition and its geological implications. Can. Mineral. 37, 525–541 v.

White, R.W., Powell, R., Clarke, G.L, 2002. The interpretation of reaction textures in Fe-rich metapelitic granulites of the Musgrave Block, central Australia: constraints from mineral equilibria calculations in the system K_2O–FeO–MgO–Al_2O_3–SiO_2–H_2O–TiO_2–Fe_2O_3. J. Metamorph. Geol. 20, 41–55. https://doi.org/10.1046/j.0263-4929.2001.00349.x v.

White, R.W., Powell, R., Holland, T.J.B., Johnson, T.E., Green, E.C.R., 2014a. New mineral activity-composition relations for thermodynamic calculations in metapelitic systems. J. Metamorph. Geol. 32, 261–286. https://doi.org/10.1111/jmg.12071 v.

White, R.W., Powell, R., Johnson, T.E., 2014b. The effect of Mn on mineral stability in metapelites revisited: new a–x relations for manganese-bearing minerals. J. Metamorph. Geol. 32, 809–828 v.

Whitney, D.L., Evans, B.W., 2010. Abbreviations for names of rock-forming minerals. Am. Mineral. 95, 185–187. https://doi.org/10.2138/am.2010.3371 v.

Wiedenbeck, M., Allé, P., Corfu, F., Griffin, W.L., Meier, M., Oberli, F., Von Quadt, A., Roddick, J.C., Spiegel, W., 1995. Three natural zircon standards for U-Th-Pb, Lu-Hf, trace element and REE analyses. Geostandards Newsletter 1–23.

Woodhead, J.D., Hergt, J.M., 2001. Strontium, neodymium and lead isotope analyses of NIST Glass certified reference materials: SRM 610, 612, 614. Geostand. Geoanal. Res. 25, 261–266. https://doi.org/10.1111/j.1751-908X.2001.tb00601.x v.

Wu, L.-G., Li, Y., Jollands, M.C., Vermeesch, P., Li, X.-H., 2022. Diffuser: A user-friendly program for diffusion chronometry with robust uncertainty estimation. Comput. Geosci. 163, 105108. https://doi.org/10.1016/j.cageo.2022.105108 v.

Xiang, H., Connolly, J.A.D., 2022. GeoPS: an interactive visual computing tool for thermodynamic modelling of phase equilibria. J. Metamorph. Geol. 40, 243–255. https://doi.org/10.1111/jmg.12626 v.

Yakymchuk, C., 2017. Applying phase equilibria modelling to metamorphic and geological processes: recent developments and future potential. Geosci. Canada 44, 27. https://doi.org/10.12789/geocanj.2017.44.114 v.